# 2nd Advanced Optical Metrology Compendium

**The latest eBook from Advanced Optical Metrology. Download for free.**

This compendium includes a collection of optical metrology papers, a repository of teaching materials, and instructions on how to publish scientific achievements.

With the aim of improving communication between fundamental research and industrial applications in the field of optical metrology we have collected and organized existing information and made it more accessible and useful for researchers and practitioners.

# RESEARCH ARTICLE

# Effects of Powder Atomization Route and Post-Processing Thermal Treatments on the Mechanical Properties and Fatigue Resistance of Additively Manufactured 18Ni300 Maraging Steel

*Faraz Deirmina, Paul A Davies,\* and Riccardo Casati\**

In this work the effect of microstructural homogenization and solution annealing prior to ageing on mechanical properties and fatigue resistance of 18Ni300 maraging steel parts processed by laser powder bed fusion (L-PBF), using two different feedstock powders with different N and O contents is investigated. The static mechanical properties are not significantly affected by the selection of the different feedstock powders. This is ascribed to the extremely fine size of the nonmetallic inclusions, characteristic of L-PBF process, even by using feedstock powders containing higher O and N contents. The tensile properties in both "directly aged," and "homogenized, solution annealed and aged" samples are comparable. The tensile strength and ductility are slightly improved compared with the vacuum melted wrought counterparts. The dynamic mechanical properties are affected by the O and N contents of the powders. Heat treatment schedule imposed a significant effect on the fatigue properties. The obtained fatigue strength in directly aged samples is already comparable to the wrought counterparts. Fatigue resistance is improved by using feedstock powders with lower oxygen and nitrogen levels. Proper homogenization heat treatments prior to ageing led to a further improvement of fatigue strength because of the elimination of intercellular microsegregation.

F. Deirmina
Powder R&D
Sandvik Additive Manufacturing AB
Mossvägen 10, Sandviken 811 82, Sweden

P. A. Davies
Powder Group
Sandvik Additive Manufacturing
Milland Road, Neath, UK
E-mail: Paul.A.Davies@sandvik.com

R. Casati
Department of Mechanical Engineering
Politecnico di Milano
Milano 20156, Italy
E-mail: Riccardo.Casati@Polimi.it

The ORCID identification number(s) for the author(s) of this article can be found under https://doi.org/10.1002/adem.202101011.

## 1. Introduction

Maraging steels comprise Fe–Ni martensitic matrix with very low carbon content. Mechanical properties of martensite are further improved by the precipitation of nanosized intermetallic particles such as $Ni_3Ti$, $Ni_3Mo$, and $Fe_7Mo_6$ μ phase upon ageing.[1,2] In recent years, several ultrahigh strength Fe–18Ni–Co–Mo quaternary alloys with additions of supplementary hardening elements (e.g., Ti) have been developed on an industrial scale.[3] In this respect, 18Ni300 with a nominal chemical composition of 18.0Ni–10.0Co–5.0Mo–0.7Ti, Fe bal. (wt%) is one of the most well-established grades in tooling applications. Additive manufacturing (AM) is a fast-growing industrial technology offering design freedom to fabricate tools with optimized design such as dies with intricate cooling channels, and forming and trimming tools.[4,5] Among AM processing technologies, laser powder bed fusion (L-PBF) has been the most used in metal AM industry.[6,7] Low-C maraging steels, due to the excellent weldability and negligible dimensional changes upon heat treatment, are among the most promising candidate alloys for commercial use in laser based AM technologies.[8,9] On an industrial scale, 18Ni300 has been in commercial use for more than a decade.[10]

The microstructure of the L-PBF processed 18Ni300 is usually composed of a martensitic matrix and an ultrafine cellular solidification structure with high dislocation density because of rapid solidification. The intercellular microsegregation usually results in chemical stabilization of retained austenite (RA) up to 11 vol% at the cell boundaries.[4] The resulting microstructure completely differs from that of conventionally processed 18Ni300 counterpart, showing a fully martensitic microstructure in solution annealed condition. Direct ageing of the L-PBF 18Ni300 from the as built state results in a larger amount of austenite (i.e., RA+ reverted austenite during ageing) than that of solution annealed and aged counterpart. Bajaj et al.[4] in their review on steels for AM, reported that the strength of the age-hardened L-PBF 18Ni300 is similar to that of conventionally processed part, concluding that the larger vol% of softer austenite in the former

**ADVANCED
SCIENCE NEWS**

www.advancedsciencenews.com

**ADVANCED
ENGINEERING
MATERIALS**

www.aem-journal.com

does not lead to significant changes in tensile strength. Ductility of directly aged AM 18Ni300 is usually lower than that of "solution annealed and aged," forged counterpart because of the presence of processing related defects, such as porosity.[11]

Wrought 18Ni300 shows a maximum hardness of ≈600 HV, and UTS of ≈2000 MPa (≈300 ksi), thus the fatigue strength at $10^6$ cycles is expected, at least empirically, at ≈1000 MPa (i.e., ≈0.5 UTS).[12,13] However, the fatigue strength at $10^6$ cycles was reported to be around 600 and ≈800 MPa for 18Ni grade steel produced by vacuum melting, and vacuum induction melting followed by vacuum arc remelting (VIM-VAR), respectively.[13–16] This poor fatigue behavior at high strength (hardness) levels has been attributed to the presence of nonmetallic inclusions (e.g., TiN, Ti-, and Al-rich oxides) which become a significant cause of fatigue limit decrease in 18Ni300 when the steel hardness is above ≈500 HV.[17] Moreover, high fatigue crack growth (FCG) rate, and extensive cyclic softening during fatigue tests due to the dislocation rearrangement and dislocation–precipitate interaction has been reported as other plausible causes for the poor fatigue strength of 18Ni300.[13–16] For more demanding applications, where fatigue strength, toughness, or improved cleanliness are of significant importance, usually VIM-VAR process is recommended to minimize the oxygen and nitrogen levels in the product.[18] The fatigue life of the directly aged AM 18Ni300 is usually lower than that of conventionally produced steel. Fatigue cracks are reported to initiate either at defects (e.g., gas pores, lack of fusion, and *nonmetallic inclusions*) or *cell boundaries* where retained/reverted austenite exists.[19,20] Pores and lack of fusion defects are L-PBF process-related and can be improved through optimization of processing parameters. The amount of the *nonmetallic inclusions* in the form of oxides and nitrides are governed by the initial N and O content of the feedstock powder, and by the atmosphere during L-PBF. The phase constitutions and microstructural features (i.e., intercellular microsegregation) can be homogenized by a proper heat treatment schedule, including homogenization and solution annealing of the as built parts prior to age hardening.[10]

The aim of the present work is to study the mechanical properties of the L-PBF 18Ni300 using two feedstock powders with different N and O contents, subjected to two post processing thermal treatments, namely (i) direct ageing from the as built condition and (ii) homogenization and solution annealing followed by ageing.

## 2. Experimental Section

For the fabrication of parts, two batches of spherical 18Ni300 maraging steel powders with a particle size distribution of (+15 μm/−53 μm) were used. Both powders were manufactured using Sandvik Osprey's proprietary inert gas atomizing technology. In this respect, a batch of powder was manufactured using vacuum induction melting, and inert gas (Ar) atomization (VIGA), while the second batch was manufactured using inert gas atomization (IGA). The chemical compositions of the starting powders are listed in **Table 1**. The main difference in the two batches is the N and O wt%, where the VIGA variant showed lower amount of oxygen (170 ppm vs 320 ppm) and significantly

**Table 1.** Chemical composition of the starting powders in wt%.

| Batch | Co | Ni | Mo | Ti | Cr | Mn | Si | Al | C | Fe | O[a] | N[a] |
|---|---|---|---|---|---|---|---|---|---|---|---|---|
| IGA | 9.00 | 17.70 | 4.90 | 0.75 | <0.25 | 0.07 | 0.07 | 0.10 | <0.03 | Bal. | 320 | 240 |
| VIGA | 9.10 | 17.60 | 4.90 | 0.74 | <0.25 | 0.05 | 0.06 | 0.08 | <0.03 | Bal. | 170 | <50 |

[a]Reported in PPM.

lower nitrogen levels (<50 ppm vs 240 ppm) compared with the IGA variant. Use of vacuum induction melting in VIGA process leads to a lower oxygen and nitrogen content.[18]

An EOS M290 machine with a 400W Yb-fiber laser was used to build the parts. Laser beam size was ≈80 μm, hatching distance was 110 μm, layer thickness of 40 μm was selected, and for the scanning pattern stripes (width of 5 mm) with a rotation of 67° between layers was selected. For the process optimization, the volumetric laser energy density (E) was considered (Equation (1)).

$$E = \frac{P}{\nu \times h \times t} \tag{1}$$

where $P$ is laser power (W), $\nu$ is the scanning speed (mm s$^{-1}$), $h$ is the hatch spacing (mm), and $t$ is layer thickness (mm). Process optimization was performed by printing 18 cubes (15 × 15 × 15 mm$^3$). Accordingly, test bars were built with a volumetric energy density of ≈80 J mm$^{-3}$. All samples for mechanical testing were built vertically.

For each batch of powders (hereafter called VIGA and IGA), samples were processed in a single build job. A number of as built samples (hereafter called AB) were subjected to direct ageing from the as built condition in a chamber furnace at 490 °C for 6 h and followed by air cooling (hereafter called DA). Another group of AB samples was subjected to homogenization treatment followed by solution annealing prior to ageing (hereafter called HSA). Homogenization was done at 960 °C under protective atmosphere (to avoid oxidation) for 5 h followed by rapid cooling, the following solution annealing was performed at 820 °C for 2 h followed by rapid cooling according to the work of Turk et al.[10] **Table 2** summarizes the samples codes and corresponding heat treatment parameters.

**Table 2.** Samples codes and summary of the heat treatments on 18Ni300 steel.

| Code | Gas Atomization | Homogenization Temperature [°C] | Solution Annealing Temperature [°C] | Ageing Temperature [°C] |
|---|---|---|---|---|
| AB-VIGA | VIGA | No heat treatment | | |
| AB-IGA | IGA | No heat treatment | | |
| DA-VIGA | VIGA | – | – | 490 |
| DA-IGA | IGA | – | – | 490 |
| HSA-VIGA | VIGA | 960 | 820 | 490 |
| HSA-IGA | IGA | 960 | 820 | 490 |

ADVANCED
SCIENCE NEWS
www.advancedsciencenews.com

ADVANCED
ENGINEERING
MATERIALS
www.aem-journal.com

Relative density measurements were carried out using image analysis on light optical microscope (LOM) images. Micrographs (40× magnification) were collected on carefully ground and polished cross-sections parallel to the build direction.[21] Microstructural analysis was performed using field emission gun scanning electron microscopy (FE-SEM, Zeiss Sigma, Germany) on ground, and oxide polished metallographic cross-sections. Energy-dispersive X-ray spectroscopy (EDS) spot, line scan, and elemental mapping as a semi-quantitative analysis were used to determine the chemical composition at cellular boundaries (i.e., microsegregated areas) on the AB and DA samples. This technique was also used to give an estimation of the chemical composition of the nonmetallic inclusions. Electron backscattered diffraction (EBSD) measurements were carried out using symmetry detector in the FE-SEM to reveal the presence and position of retained and reverted austenite in the microstructure of AB and the age hardened samples, respectively. Thermodynamic calculations were carried out using Thermocalc software (TCFE9 database).

Rockwell C hardness measurements were carried out on carefully ground cross-sections ($15 \times 15 \times 60\,mm^3$) in accordance with the ASTM E18 standard. Vickers hardness (HV10) measurements were carried out on ground and polished metallographic cross-sections according to the ASTM E-384 standard. An average value of at least 6 measurements is reported. Tensile tests were performed conforming to the ASTM E8M standard. Instrumented Charpy V-notch (CVN) tests were carried out according to the ASTM E2298 standard. The geometry and dimension of the specimens for rotating bending fatigue tests was according to the ISO1143 standard. Staircase approach, as a statistical method to give the standard deviation and mean fatigue endurance, was selected (ISO 12 107 standard). The rotating-bending fatigue tests were performed using Italsigma 2TM831 testing machine. Maximum number of cycles (i.e., run-out) was set to $2 \times 10^6$ cycles. Rotation speeds and load step were set to 2300 RPM and 25 MPa, respectively. All machining operations were carried out after age hardening process.

## 3. Results and Discussion

### 3.1. AB Parts

Both VIGA and IGA processed parts showed relative densities of over 99.9%. In AB condition, traces of melt pool boundaries are noticeable after chemical etching with Nital 5% (**Figure 1**a). The martensitic matrix was revealed by Kalling's reagent, columnar prior austenite grains (PAGs) are evident in the micrograph of Figure 1b. At a higher magnification, microstructure is characterized by an ultrafine cellular solidification structure (Figure 1c). Cellular boundaries are characterized by the microsegregation of alloying elements (i.e., Ni, Mo, and Ti) (**Table 3**), which lead to the chemical stabilization of retained austenite ($\approx$5 vol%), as shown in the EBSD phase map (Figure 1d).[22–25]

Fast solidification during L-PBF process can be qualitatively modeled by Scheil solidification modeling involving complete diffusion in the liquid while no diffusion in solid. The results highlight that the solidification starts with the formation of austenite (FCC_A1) (**Figure 2**a). By increase in mass fraction of the
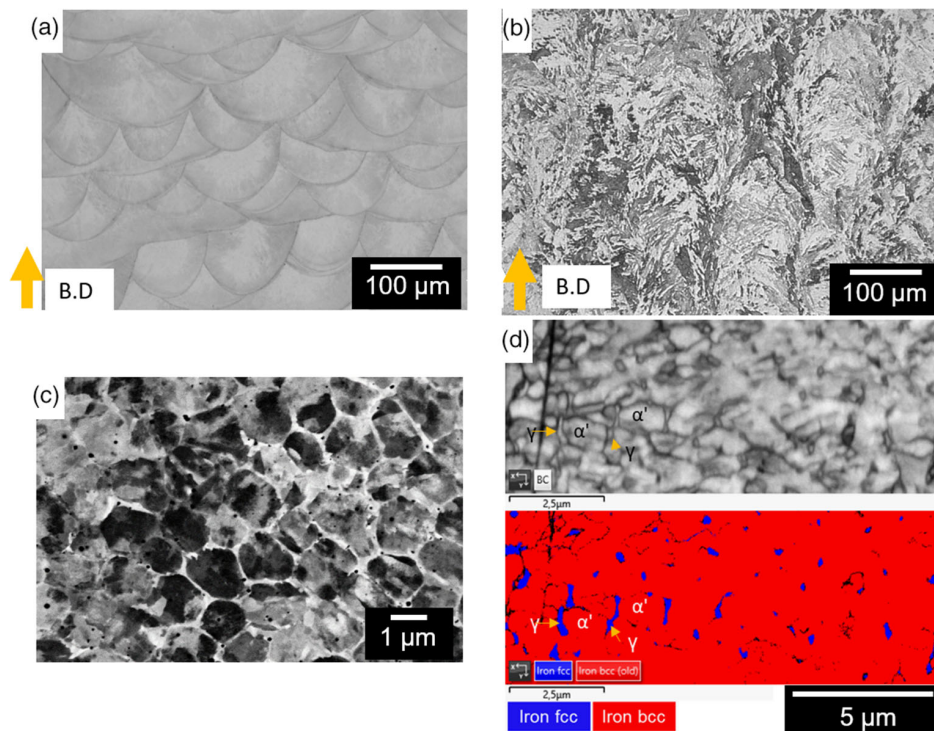


**Figure 1.** a) LOM of AB 18Ni300 steel (Nital 5%), b) LOM of AB sample (Kalling's), and c) SEM micrograph showing the ultrafine cellular structure, cell boundaries appearing brighter in BSE image, and d) EBSD band contrast image and corresponding phase maps, RA (denoted by γ) detected at the cell boundaries.

**ADVANCED
SCIENCE NEWS**

www.advancedsciencenews.com

**ADVANCED
ENGINEERING
MATERIALS**

www.aem-journal.com

**Table 3.** EDS spot analysis results on matrix and microsegregation at the cell boundaries, wt%.

| Sample | Position | Ni | Mo | Co | Ti | Al | Fe |
|---|---|---|---|---|---|---|---|
| AB-IGA | Microsegregation | $21.0 \pm 1.2$ | $6.5 \pm 0.3$ | $10.5 \pm 0.9$ | $2.2 \pm 0.2$ | $0.2 \pm 0.1$ | Bal. |
| AB-VIGA | Microsegregation | $20.8 \pm 0.9$ | $6.9 \pm 0.4$ | $10.6 \pm 0.2$ | $2.1 \pm 0.2$ | $0.1 \pm 0.1$ | Bal. |
| AB-IGA | Matrix | $18.2 \pm 1.1$ | $4.8 \pm 0.2$ | $11.0 \pm 0.8$ | $0.5 \pm 0.1$ | $0.2 \pm 0.1$ | Bal. |
| AB-VIGA | Matrix | $19.0 \pm 1.8$ | $4.2 \pm 0.4$ | $9.6 \pm 0.8$ | $0.6 \pm 0.2$ | $0.1 \pm 0.1$ | Bal. |

solid, the remaining liquid to solidify progressively enriches in alloying elements (i.e., Ni, Mo, and Ti) (Figure 2b). This is qualitatively in line with the experimental observations (Table 3) showing that the cellular boundaries (i.e., the last liquid to solidify) are heavily enriched in alloying elements. Applying the thermodynamic based martensite start (Ms) modeling by Thermocalc,[26] and using the EDS results (Table 3, AB-VIGA) as input data, Ms temperature in microsegregated areas can be as low as $\approx 20\,°C$, and the austenite to martensite transformation cannot be completed even at cryogenic temperatures (Figure 2c). Therefore, the intercellular austenite, heavily enriched in alloying elements remains stable at room temperature. This is in line with the EBSD results. For comparison, the modeling related to the matrix chemical composition is plotted. The Ms temperature is around $200\,°C$, and the transformation can be almost fully completed at room temperature in agreement with experimental dilatometry results.[27] In addition to the aforementioned discussion, it should be noted that RA islands are ultrafine in size (see Figure 1d). When austenite is cooled down, the volume expansion due to the martensitic transformation within one prior austenite grain is compensated by the formation of multi variant blocks. This is easier in larger grains than the smaller ones.[28] In other words, ultrafine austenitic grains cannot accommodate high elastic strain energy and could also remain mechanically stable.

The main difference between VIGA (**Figure 3**a) and IGA (Figure 3b) processed parts is in the relatively larger number of nonmetallic inclusions in the latter. Higher magnification SEM micrographs show that most of the nonmetallic inclusions are ultra-fine and nanosized (phases appearing darker in BSE micrographs in **Figure 4**c,d), uniformly distributed within the microstructure.

The nonmetallic inclusions are characterized as Ti- and Al-rich oxides, probably $(Ti, Al)_2O_3$ according to EDS analysis, ranging from hundreds of nanometers to some micrometers (Figure 4a). In case of IGA samples, in addition to oxides, some finer inclusions ($<500\,nm$) showing a core shell structure with Al- and Ti-rich oxides in the core and Ti(N,C) in the shell are found (Figure 4b,c). The types of nonmetallic inclusions found in this work agree well with the work of Shamsdini et al. on L-PBF 18Ni300.[29]

The nanosized spherical oxide inclusions are not as detrimental as the larger irregular ones to mechanical properties.[30] The morphology and size of oxides suggests that at certain regions of the melt pool oxides might have been formed as a result of dissolution and reprecipitation in the molten pool.[31–33] Thanks to the very fast cooling rates ($\approx 10^3$ to $10^7\,K\,s^{-1}$) of the L-PBF process,[34] either growth or oxides agglomeration is hindered, and the oxides remain nanosized. To prove this hypothesis, the authors cannot show any direct experimental evidence. However, under the assumptions made by Hong et.al.[32] on the dissolution of oxides in a weld pool [namely i) Only $Al_2O_3$ is considered as the oxide inclusion that is instantly existing as $Al_2O_3$ nuclei uniformly distributed in the molten steel, ii) the chemical composition of the molten pool is assumed to be constant, and iii) the growth and dissolution rates of the oxide is only determined by the diffusion rate of oxygen, and growth by interparticle collisions was neglected], for an $Al_2O_3$ particle with the initial diameter of $1\,\mu m$, less than $10^{-2}\,s$ is needed to completely dissolve in the melt at $2027\,°C$, while it takes $\approx 1\,s$ to dissolve the same particle at $1972\,°C$. Moreover, the time
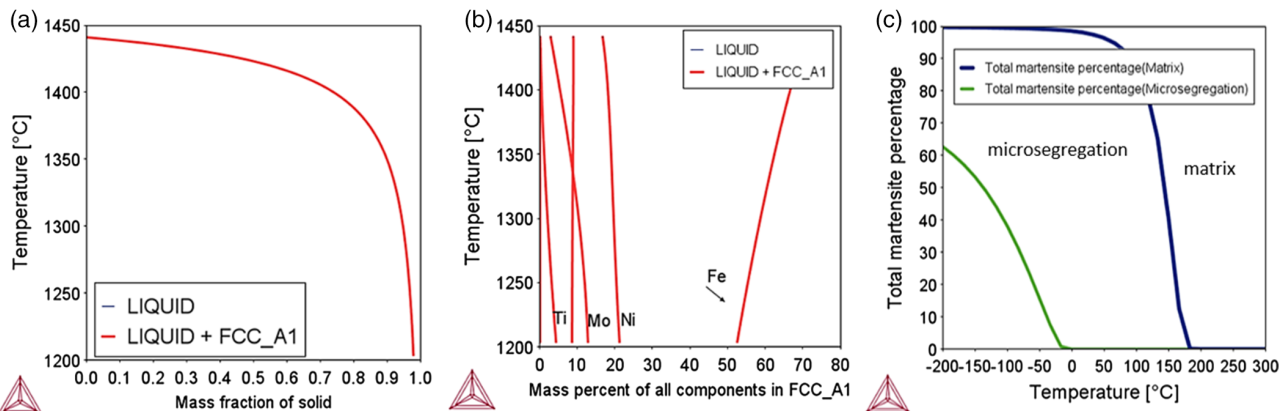


**Figure 2.** a) Mass fraction of solid versus temperature; b) mass fraction of alloying elements in liquid versus temperature calculated, using the Scheil model; and c) Ms and martensite fraction modeling: microsegregated regions versus 18Ni300 matrix.
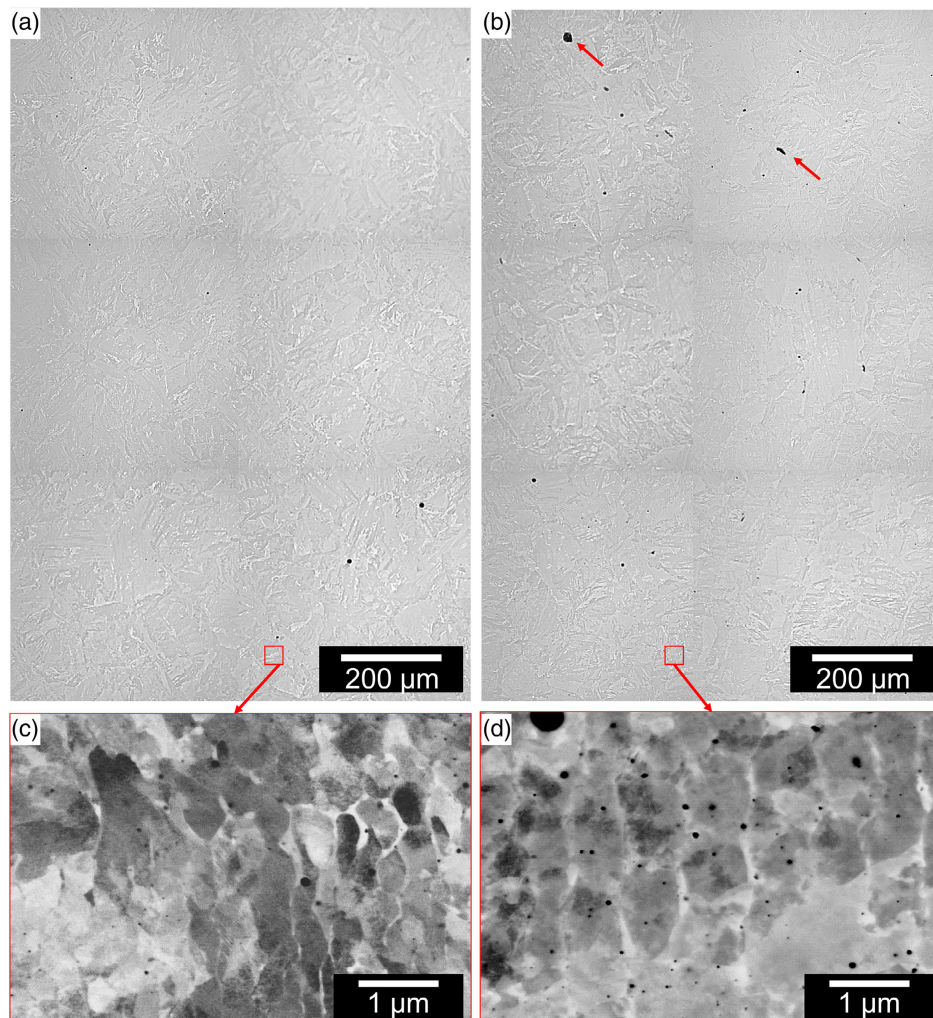
**ADVANCED
SCIENCE NEWS**

www.advancedsciencenews.com

**ADVANCED
ENGINEERING
MATERIALS**

www.aem-journal.com

**Figure 3.** LOM of a) VIGA processed part, b) IGA processed part (arrows showing inclusions), c) high magnification SEM micrographs of VIGA processed part, and d) IGA processed part, note the higher amount of nonmetallic nanosized inclusions appearing darker in back scattered electron (BSE) micrographs.

needed for complete dissolution increases drastically by increasing the oxide diameter. In other words, higher temperatures or longer times are needed to completely dissolve the coarser particles. The dissolution condition in the current work could be met in view of the melt pool effective temperature and fine size of the starting inclusions (inclusions formed during the atomization process of powders). The reprecipitation starts by cooling down, while an undercooling of approximately 50 °C is required to force nucleation. The growth of the precipitates is governed by the cooling rate.[31–33] Therefore, the extremely fast cooling rate, characteristic of L-PBF process, could probably hinder the growth of oxides. In the present study, oxides contain Al and Ti as the major constituents. This will reduce the dissolution temperature of the oxides compared with pure $Al_2O_3$. This can be inferred from the equilibrium step diagram for IGA and VIGA powders, where, at temperatures above 1750 °C, the dissolution of corundum, $(Al, Ti)_2O_3$, should start (**Figure 5**a,b). The core-shell structure of Al- and Ti-rich oxides, and Ti(N,C) was observed in IGA samples with higher nitrogen content.

In this case, it is plausible that the rapid solidification impedes the growth of the nucleated Al and Ti oxide and, at a later stage, Ti(N,C) preferentially precipitates on the nanosized oxide. These phases are also predicted in the equilibrium phase diagram (Figure 5b). The vol% of the nanosized oxides and nitrides measured by the image analysis on bulks using at least 10 micrographs (20 k magnification) selected on different areas are fairly in line with those calculated by Thermocalc using the powder chemical compositions reported in Table 1 (Figure 5c). This means that there was no significant oxygen and nitrogen pick-up during L-PBF process. The vol% of nonmetallic inclusions in VIGA samples is around 0.15, while in those produced using IGA powders this value increases to around 0.30 because of higher O and N wt% in IGA powders.

### 3.2. Homogenization and Solution Annealing

Regardless of the feedstock powder type, homogenization thermal treatments lead to the formation of equiaxed PAGs as
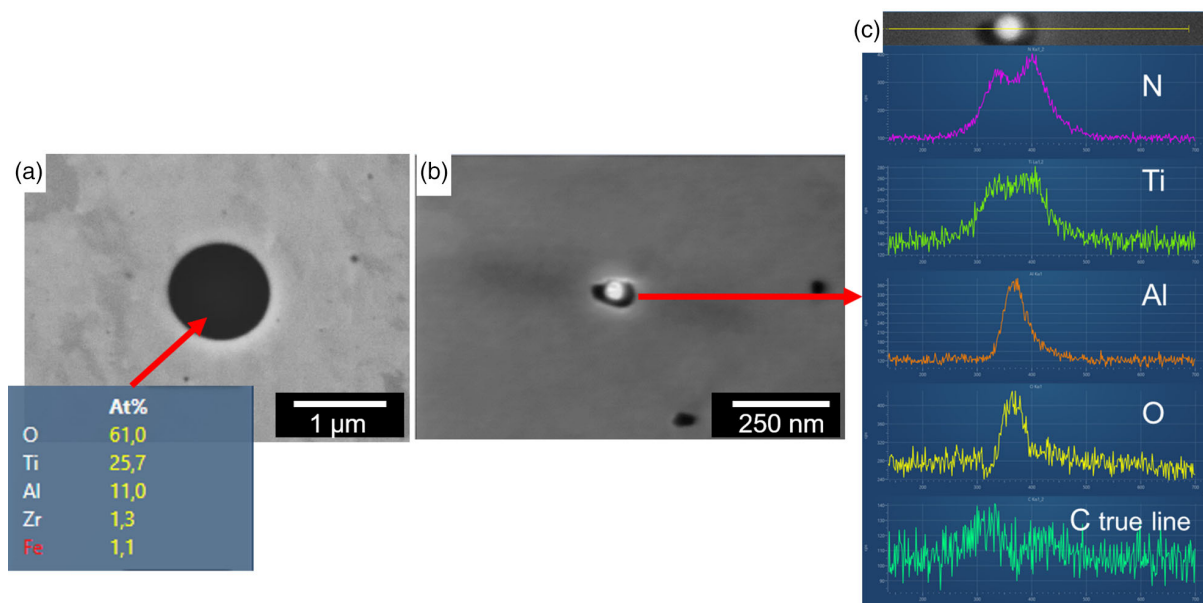
**Figure 4.** a) EDS spot analysis on a micron-sized oxide (VIGA) in at%, and b) In-lens micrograph of a nanosized inclusion, and c) corresponding EDS line scan on the nanosized inclusion showing an oxide core, served as later nitride precipitation (IGA).
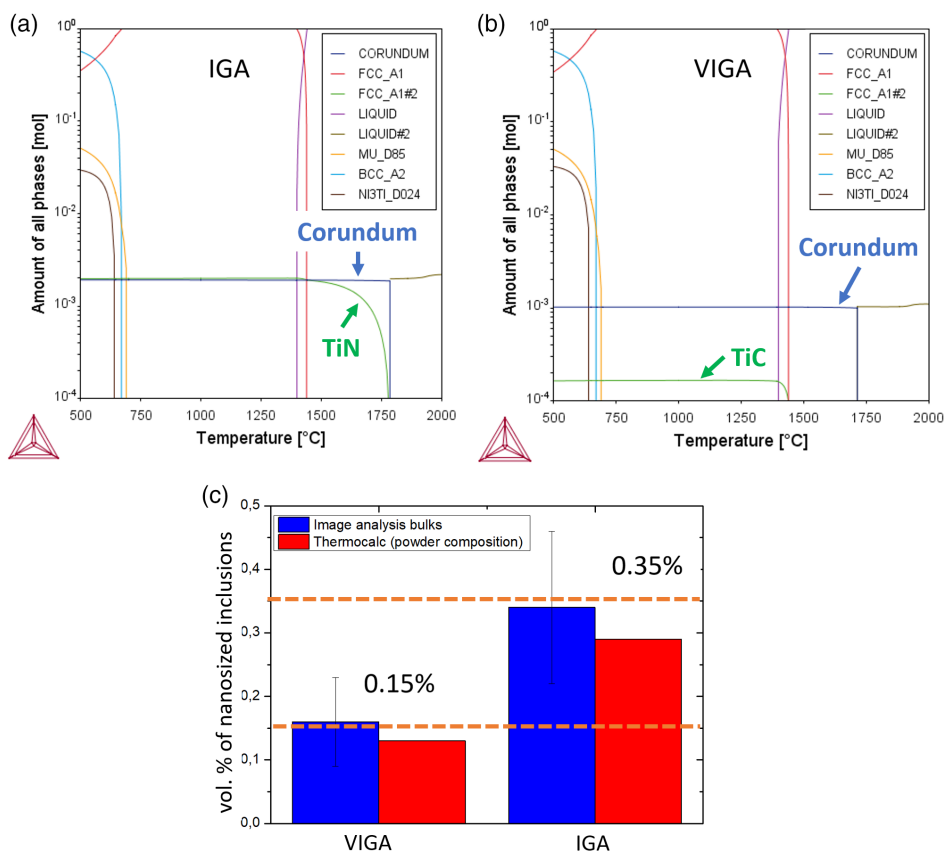


**Figure 5.** Equilibrium property diagrams of a) IGA and b) VIGA powders, and c) vol% of nonmetallic inclusions predicted by Equilibrium property diagrams and image analysis for VIGA and IGA processed parts.
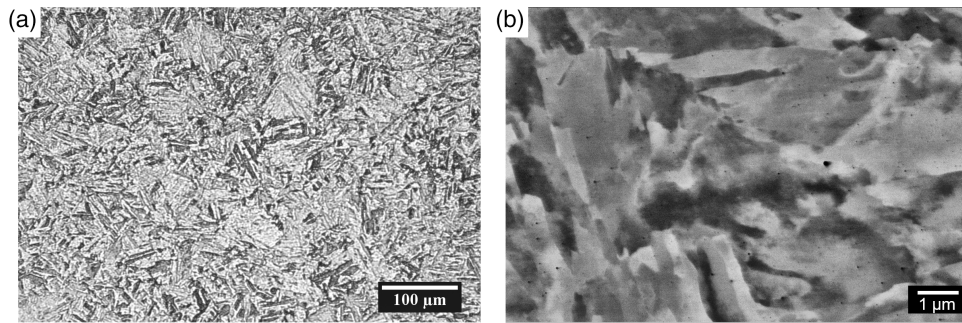
**ADVANCED
SCIENCE NEWS**

www.advancedsciencenews.com

**ADVANCED
ENGINEERING
MATERIALS**

www.aem-journal.com

**Figure 6.** Microstructure after homogenization and solution annealing a) LOM (Kalling's reagent), b) SEM micrograph showing the martensitic microstructure.

depicted in **Figure 6**a (see Figure 1b for comparison). The microstructure is martensitic, and the inter-cellular microsegregation is homogenized due to enhanced diffusivity at high temperature as shown in Figure 6b (see Figure 1c for comparison). Consequently, no RA is detected in the homogenized and solution annealed samples similar to the wrought material in solution annealed condition.[35]

### 3.3. Ageing

The age hardened microstructure of both DA-VIGA and DA-IGA samples comprise the prior cellular solidification structure (**Figure 7**a), nanosized precipitates (Figure 7c), and an increased amount of austenite (≈7 vol% vs 5 vol% in AB state) at the cellular boundaries due to the preferential growth of reverted austenite on the intercellular RA during ageing (Figure 7e). In HSA samples, a coarsening of martensite substructure (e.g., blocks and laths) due to high temperature homogenization prior to ageing is evident (Figure 7b), and intermetallic nanoprecipitates emerge after ageing (Figure 7d). Except for a small vol% of reverted austenite at the martensite sub-structure boundaries, no significant austenite is found in the microstructure (Figure 7f). It should be noted that in 18Ni300, austenite is an equilibrium phase at the ageing temperature interval,[35] (see also austenite (FCC_A1) stability temperature in Figure 5a,b). Therefore, during isothermal ageing, the system approaches equilibrium leading to austenite nucleation from the metastable Fe–Ni martensite through a diffusion-controlled reaction (i.e., austenite reversion).

### 3.4. Hardness and Mechanical Properties

The hardness of the AB materials is around 385 HV10, this value dropped to around 315 HV10 after homogenization and solution annealing. This can be ascribed to dislocation recovery and possibly martensite sub-structure coarsening.[36] However, in both cases, 6 h ageing at 490 °C results in a significant increase in hardness to ≈580 HV10 (53–54 HRC) as a result of intermetallic nanoprecipitation. The HSA samples from both powder variants show slightly higher hardness numbers than those of DA counterparts. **Table 4** summarizes hardness and the mechanical properties of the samples. The tensile strength of AB parts produced with IGA and VIGA powders is similar (≈1240 MPa), while the

elongation, area reduction and impact toughness of VIGA samples (i.e., 17.9%, 68%, and 108.0 J, respectively) are higher than those of IGA samples (i.e., 17.1%, 63%, and 63.0 J, respectively). A significant drop in dynamic mechanical property (i.e., impact toughness) in IGA processed parts can be ascribed to the higher number of nonmetallic inclusions. Age hardened samples, irrespective of feedstock powder and postprocessing thermal treatment schedule, show tensile strength values higher than 2000 MPa. This is accompanied by a reduction in ductility and impact toughness. DA-VIGA and DA-IGA steels show similar tensile strength (2030 MPa). However, DA-VIGA samples show higher elongation, area reduction and impact toughness (i.e., 9.2%, 45%, and 17.0 J, respectively) than the DA-IGA ones (i.e., 7.2%, 34%, and 12.0 J, respectively). This can be due to the lower O and N content in the former, leading to smaller vol% of nonmetallic inclusions. Homogenization and solution annealing prior to ageing, generally result in slightly improved mechanical properties. The HSA-IGA samples show higher tensile strength (i.e., 2111 MPa), elongation, area reduction, and impact toughness (i.e., 9.0%, 40%, and 13.5 J, respectively), compared with DA-IGA counterparts. However, in case of HSA-VIGA alloy, tensile strength is marginally improved (i.e., 2070 MPa) at the expense of ductility and impact toughness. Generally, by increasing the tensile strength and hardness, due to elimination of softer RA phase in HSA samples, one would expect a slight reduction in ductility and impact toughness. The opposite behavior witnessed in IGA variants is likely due to the presence of nanosized oxides impeding the prior austenite grain growth after recrystallization, during the high temperature homogenization treatment. This might lead to an increase in impact toughness,[37] which should be further studied. Regardless of the powder type and post processing thermal treatment, all AM parts show similar or even improved properties compared with the wrought 18Ni300 maraging steel (Table 4). These results highlight the capability of L-PBF to produce fine microstructure materials and to hinder growth and agglomeration of nonmetallic inclusions stemming from the alloying elements (i.e., Ti and Al) that show high affinity for O and N. Strict control on the vol% and size of inclusions is reported to be hard in wrought 18Ni300, especially in the absence of VIM-VAR process.[18,38]

Fracture surfaces of the tensile specimens in the AB and aged condition (**Figure 8**a,b, respectively) show a cup-cone fracture
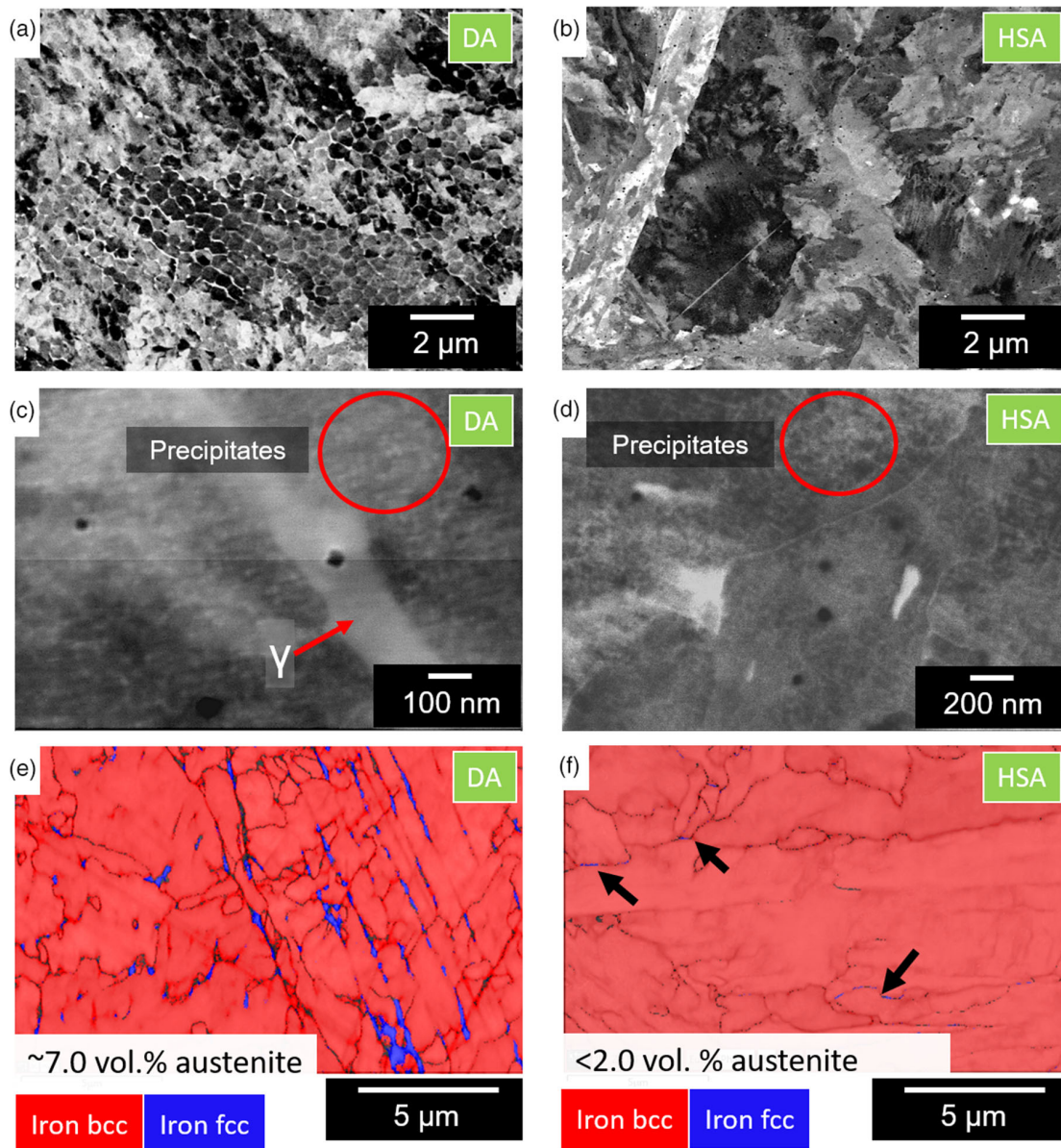
**Figure 7.** a) SEM micrographs of DA sample, b) SEM micrographs of HSA sample, c) higher magnification micrograph of DA, showing the traces of nanoprincipates, and intercellular austenite (denoted by γ), d) higher magnification micrograph of HSA showing the traces of nanoprincipates, e) EBSD band contrast image overlaid by phase maps, austenite (RA+ reverted austenite) detected at the cell boundaries in DA samples, and f) EBSD band contrast image overlaid by phase maps, austenite reversion detected at the block and lath boundaries in HSA samples (arrows).

morphology indicative of the ductile fracture, where the area reduction in softer AB sample is significantly larger than that of the harder aged one.

### 3.5. High Cycle Fatigue

Fatigue test results obtained by staircase method are summarized in **Figure 9** and **Table 5**. The fatigue properties are affected more significantly by the selection of powder variants. At a similar hardness and tensile strength (see Table 4), DA-VIGA showed higher mean fatigue strength than that of DA-IGA (i.e., 700 vs 570 MPa). Homogenization and solution annealing prior to

ageing give rise to higher mean fatigue strength in both variants (i.e., 717 and 750 MPa for HSA-IGA and HSA-VIGA, respectively). An increase of 125 MPa in minimum fatigue strength is evident in DA-VIGA steel compared with that of DA-IGA steel, the minimum attainable fatigue strength is increased for both IGA and VIGA samples in HSA condition in comparison with DA counterparts. This value is around 50 and 125 MPa for VIGA and IGA alloy, respectively (Figure 9a–d). The fatigue strength results are comparable or even higher than those of wrought 18Ni300 steel[13,39] (Table 5).

The fatigue crack initiated at a near surface defect (**Figure 10**a and inset), surface (Figure 10b and inset), or an oxide inclusion

ADVANCED
SCIENCE NEWS

www.advancedsciencenews.com

ADVANCED
ENGINEERING
MATERIALS

www.aem-journal.com

**Table 4.** Summary of the mechanical properties.

| | Yield Strength [MPa] | Tensile strength [MPa] | Elongation [%] | Area Reduction [%] | Hardness HV10/HRC | CVN, Impact toughness [J] | Ref. |
|---|---|---|---|---|---|---|---|
| **VIGA** | | | | | | | |
| VIGA-AB | 1181 ± 4 | 1242 ± 2 | 17.9 ± 0.1 | 68 ± 2 | 385 ± 6/39 | 108.0 | This work |
| DA-VIGA | 1974 ± 5 | 2031 ± 4 | 9.2 ± 0.2 | 45 ± 1 | 580 ± 4/54 | 17.0 | This work |
| HSA-VIGA | 1970 ± 40 | 2071 ± 30 | 8.3 ± 0.8 | 37 ± 3 | 594 ± 7/54 | 14.0 | This work |
| **IGA** | | | | | | | |
| IGA-AB | 1172 ± 4 | 1244 ± 5 | 17.1 ± 0.5 | 63 ± 1 | 385 ± 10/39 | 63.0 | This work |
| DA-IGA | 1961 ± 10 | 2029 ± 9 | 7.2 ± 1.2 | 34 ± 5 | 575 ± 5/53 | 12.0 | This work |
| HSA-IGA | 2008 ± 16 | 2111 ± 15 | 9.0 ± 0.3 | 42 ± 2 | 585 ± 5/54 | 13.5 | This work |
| **Wrought** | | | | | | | |
| VIM/VAR | 1800–1900 | 1900–2100 | 9.0 | 40 | NR | NR | [47] |
| Vacuum melted | 2000 | 2050 | 7.0 | 40 | NR | NR | [38] |
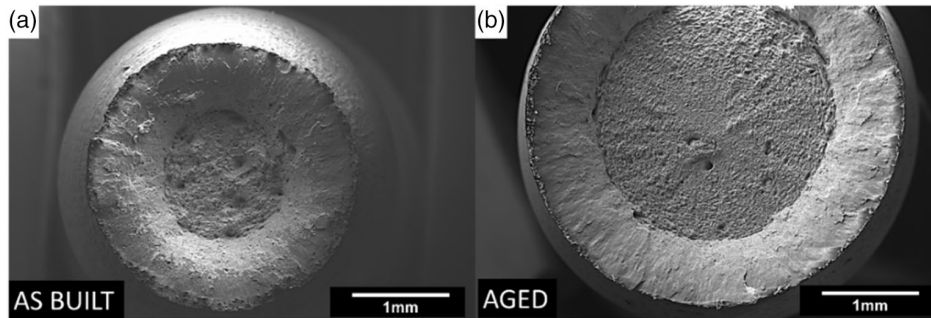


**Figure 8.** SEM micrographs on fracture surface of the a) AB and b) aged sample.
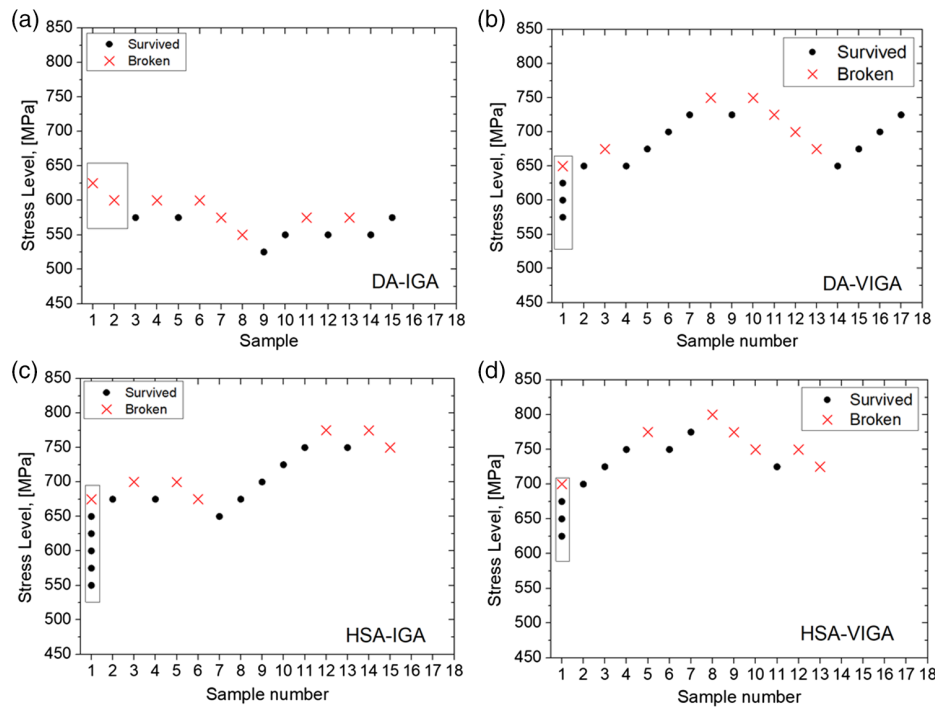


**Figure 9.** Experimental data of fatigue tests: a,b) DA, c,d) HSA samples, note that the data in square are not considered as suggested by ISO12107 standard.

**Table 5.** Summary of the fatigue results.

| Age hardened samples | Fatigue strength[a] [MPa] | Test Configuration/cycles | Ref. |
|---|---|---|---|
| **VIGA** | | | |
| DA-VIGA | $700 \pm 65$ | Rotating Bending/$2 \times 10^6$ | This work |
| HSA-VIGA | $750 \pm 38$ | Rotating Bending/$2 \times 10^6$ | This work |
| **IGA** | | | |
| DA-IGA | $570 \pm 20$ | Rotating Bending/$2 \times 10^6$ | This work |
| HSA-IGA | $717 \pm 100$ | Rotating Bending/$2 \times 10^6$ | This work |
| **Wrought 18Ni300** | | | |
| VIM/VAR | $>735$ | Bending/$1 \times 10^7$ | [47] |
| Vacuum melted Aged to $\approx 560$ HV | 700 | Tension-Compression/$2 \times 10^6$ | [13] |
| Vacuum melted Aged to $\approx 600$ HV | $600 \pm 30$ | Rotating Bending/$2 \times 10^6$ | [39] |

[a]Mean and standard deviation is calculated according to ISO 12 107 standard.

near the surface (Figure 10c,d). In all cases, the fracture surface is characterized by crack initiation zone, fatigue fracture region, and finally overload fracture. This is shown in the BSE micrograph in Figure 10a.

### 3.5.1. Directly Aged Condition

A defect-free (i.e., inclusion-free and fully dense) matrix of ultrahigh strength steel should show an intrinsic fatigue limit which is proportional to the hardness or UTS. This intrinsic fatigue limit can be obtained if the size of defects is smaller than a critical value. Lower fatigue limit values of ultrahigh strength steels are thus caused by defects, as crack initiators (see Figure 10a,c), larger than a critical value. The critical defect size varies with the hardness of the steel.[17] In this condition, according to Murakami and Endo,[40] a geometrical parameter (i.e., square root of the defect area, such as a pore or nonmetallic inclusion projected on a plane perpendicular to the stress direction, $\sqrt{area}$), and the hardness of the part (HV) govern the fatigue limit ($\sigma$w).Three distinct equations can be derived for the surface, substrate and internal defects initiating the fatigue failure, and are well applied to AM components[41] (Equation (2)–(4))

$$\sigma_{w, surface} = \frac{1.43(HV + 120)}{(\sqrt{area})^{\frac{1}{6}}} \tag{2}$$

$$\sigma_{w, substrate} = \frac{1.40(HV + 120)}{(\sqrt{area})^{\frac{1}{6}}} \tag{3}$$

$$\sigma_{w, internal} = \frac{1.56(HV + 120)}{(\sqrt{area})^{\frac{1}{6}}} \tag{4}$$

With reference to Equation (2)–(4) and in view of the similar hardness and tensile strength of DA-IGA and DA-VIGA (Table 4), the higher fatigue strength in DA-VIGA can be correlated with the lower number of defects and smaller defect size (i.e., $\sqrt{area}$).[42] Therefore, given the statistical nature of the staircase fatigue test method, it is possible to conclude that the higher fatigue strength of VIGA variants is a result of the lower O, and N content in the starting powders which ultimately leads to a smaller vol%, and possibly finer size of the nonmetallic inclusions in the matrix. Moreover, the lower vol% of
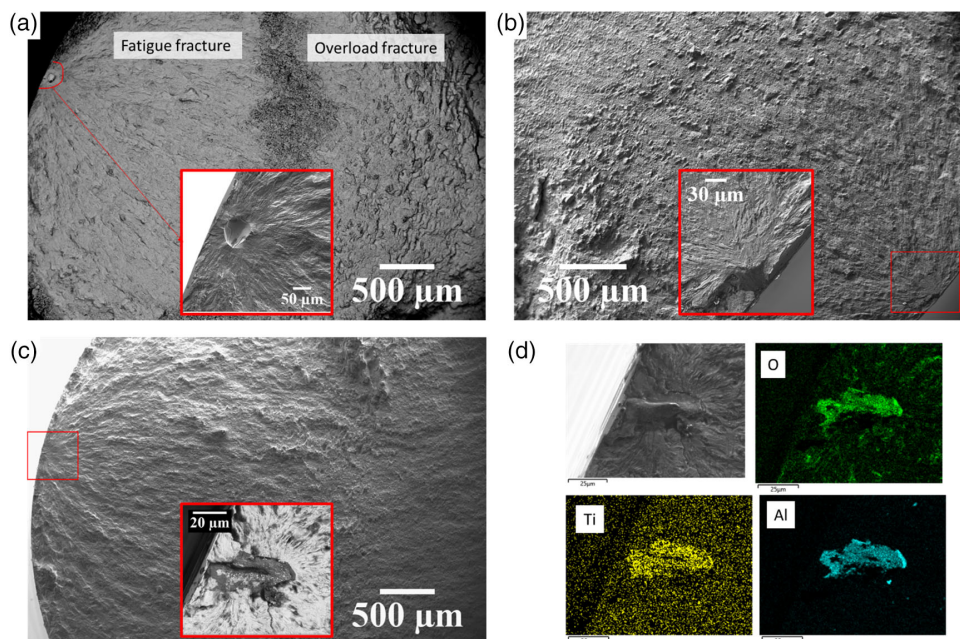


**Figure 10.** a) Fracture surface of DA VIGA (sample 12) showing crack initiation near the surface from a defect (probably gas pore), fatigue fracture and overload fracture regions, b) fracture surface of HSA IGA (sample 15) showing initiation of the fatigue crack on the surface, c) fracture surface of DA VIGA (sample 13) showing an oxide inclusion initiating the fatigue crack, and d) corresponding EDS elemental mapping of the oxide inclusion.

inclusions in DA-VIGA reduces the probability of the existence of a fatal defect near the surface of the test bars compared with DA-IGA. This is also reflected in the minimum fatigue strength values obtained for these two batches, where DA-VIGA shows a minimum fatigue strength 125 MPa higher than that of DA-IGA.

### 3.5.2. Effect of Homogenization and Solution Annealing on Fatigue Strength

The fatigue strength evaluated by the staircase method is a statistical value, and for each batch of powders (i.e., VIGA and IGA), all the specimens (i.e., DA and HSA) were L-PBF processed together in a single job, and machined using the same equipment. Therefore, from a statistical viewpoint, $\sqrt{area}$ (defect size) should be similar for both DA and HSA samples processed using the same powder batch. Moreover, the tensile strength and hardness of the HSA parts were almost similar to those of DA counterparts. In this case, Equation (2)–(4) should predict a fairly similar fatigue strength for HSA and

DA parts, if the global hardness, and defect size are taken into account. Therefore, the statistically meaningful higher fatigue strength in HSA parts should be discussed in view of the matrix resistance to the fatigue crack propagation. This can be directly linked to the different microstructural features of DA and HSA samples.

The fatigue fracture region in DA samples (**Figure 11**) is characterized by the secondary cracking, shown by arrows, along intercellular austenite (microsegregated regions shown by EDS elemental mapping). Intercellular austenite is much softer than the martensitic matrix. In this condition, crack opening leads to stress induced martensitic transformation in the intercellular austenite. This is shown by EBSD analysis near the fatigue crack propagation path (see **Figure 12**a,b) where the intercellular austenite is fully transformed to martensite at the vicinity of the fatigue crack propagation path. In lower strength steels (e.g., transformation induced plasticity (TRIP) maraging steels), the stress assisted martensitic transformation is responsible for energy dissipation, volume expansion as well as work hardening at a fatigue crack tip.[43] This reduces the driving force for crack
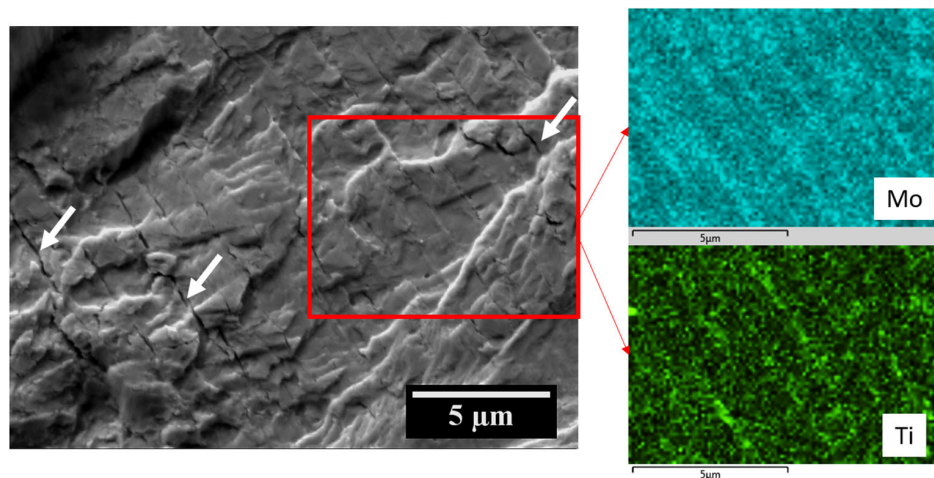


**Figure 11.** Secondary cracks along intercellular/interdendritic regions at the fatigue fracture zone, note the higher Mo and Ti concentration by EDS mapping.
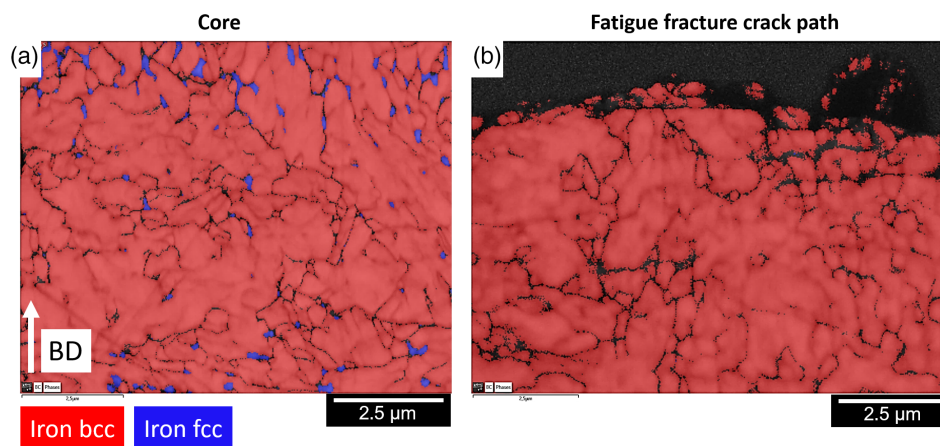


**Figure 12.** EBSD scans on DA VIGA sample number 8, a) band contrast image overlaid by phase maps on area far from fracture surface, and b) band contrast image overlaid by phase maps on the crack propagation path, note the absence of austenite.

propagation (positive effect).In contrast, there might be two negative effects associated with the ultrafine intercellular austenite in an ultrahigh strength martensitic matrix such as 18Ni300. First, similar to observations by Ran et al.,[44] with the increase of stress intensity factor ($\Delta K$), coalescence of sub-cracks (secondary cracks) along softer inter-cellular austenite, with the main crack, can accelerate FCG rate. Indeed, at high ($\Delta K$), intercellular austenite could accelerate the FCG rate.[44] Moreover, Nakagawa and Miyazaki[45] reported that retained austenite was not beneficial to the fatigue limit of a precipitation hardening martensitic stainless steel. Second, given the intercellular austenite size in this study (i.e., $\approx 0.5\,\mu m^2$ in area, see Figure 1d and 12a), the stress assisted transformation occurs with much lower required energy, because the small size geometrically impedes the activation of mechanical twining before the transformation, leading to transformation even at small deformations.[46] Therefore, the positive effect of phase transformation must have been cancelled-out by the fact that the fatigue crack could propagate much easier along the locally "softer" austenite or austenite/matrix interface compared with much harder martensite in this alloy. Therefore, the statistically meaningful increase of the fatigue strength in HSA samples can be discussed in view of the elimination of intercellular austenite, and austenite/matrix interface serving as locally weak sites for the propagation of fatigue crack by microcrack formation, and their coalescence, leading to an increased fatigue crack propagation rate.[44]

## 4. Conclusions

In this article, the mechanical properties of the L-PBF 18Ni300 alloys produced with two feedstock powders (with different N and O contents) and subjected to different heat treatment schedules (namely, i) direct ageing and ii) homogenization, solution annealing followed by ageing) were investigated. The following conclusions can be drawn: 1) Larger O and N wt% in IGA samples, led to a higher vol% of nonmetallic inclusions in the form of complex oxides and titanium nitride. However, thanks to the L-PBF process characteristics, most of the nonmetallic inclusions remained nanosized with no significant effect on ductility and toughness. This led to the achievement of tensile properties similar to the wrought counterparts. 2) AB microstructure comprised martensite and intercellular RA due to the microsegregation of alloying elements during fast solidification. Homogenization at high temperature removed the RA and led to a fully martensitic microstructure. 3) In directly aged samples, austenite reversion during ageing took place in the intercellular regions, while in homogenized and solution annealed samples, austenite nucleated at martensite substructure boundaries. 4) Regardless of the feedstock powder and post processing thermal treatment selection, hardness, and tensile properties of L-PBF processed 18Ni300 were equal or slightly improved compared with the wrought 18Ni300. This improvement was more pronounced when using VIGA powders. 5) The fatigue strength was affected more significantly by the selection of powder variants. Directly aged VIGA samples showed higher fatigue strength than that of directly aged IGA ones (i.e., 700 vs 570 MPa), as a result of lower number of nonmetallic inclusions (i.e., crack initiators). 6) Homogenization and solution annealing prior to ageing gave rise to higher achievable fatigue strength in both variants (i.e., 717 and 750 MPa for HSA-IGA and HSA-VIGA, respectively). This behavior was discussed in view of the elimination of intercellular austenite (softer than the aged martensite) in HSA samples. 7) The fatigue properties, using both atomization routes, was comparable (IGA) or slightly improved (VIGA) in comparison with the results found in literature for the wrought 18Ni300.

## Conflict of Interest

The authors declare no conflict of interest.

## Data Availability Statement

Research data are not shared.

[1] R. Tewari, S. Mazumder, I. S. Batra, G. K. Dey, S. Banerjee, *Acta Mater.* **2000**, *48*, 1187.

[2] V. K. Vasudevan, S. J. Kim, C. M. Wayman, *MTA* **1990**, *21*, 2655.

[3] A. M. Hall, C. J. Slunder, *The Metallurgy, Behavior, and Application of the 18-Percent Nickel Maraging Steels*, Battelle Memorial Inst., Columbus OH **1968**.

[4] P. Bajaj, A. Hariharan, A. Kini, P. Kürnsteiner, D. Raabe, E. A. Jägle, *Mater. Sci. Eng. A* **2020**, *772*, 138633.

[5] T. Skåre, N. Asnafi, *IOP Conf. Ser.: Mater. Sci. Eng.* **2020**, *967*, 012040.

[6] W. E. Frazier, *J. Mater. Eng. Perform.* **2014**, *23*, 1917.

[7] L. Hitzler, M. Merkel, W. Hall, A. Öchsner, *Adv. Eng. Mater.* **2018**, *20*, 1700658.

[8] S. Amirabdollahian, F. Deirmina, L. Harris, R. Siriki, M. Pellizzari, P. Bosetti, A. Molinari, *Scr. Mater.* **2021**, *201*, 113973.

[9] K. Kempen, E. Yasa, L. Thijs, J.-P. Kruth, J. Van Humbeeck, *Phys. Proc.* **2011**, *12*, 255.

[10] C. Turk, H. Zunko, C. Aumayr, H. Leitner, M. Kapp, *Berg. Huettenmaenn. Monatsh.* **2019**, *164*, 112.

[11] S. Yin, C. Chen, X. Yan, X. Feng, R. Jenkins, P. O'Reilly, M. Liu, H. Li, R. Lupoi, *Addit. Manuf.* **2018**, *22*, 592.

[12] W. Wang, W. Yan, Q. Duan, Y. Shan, Z. Zhang, K. Yang, *Mater. Sci. Eng. A* **2010**, *527*, 3057.

[13] L. F. Van Swam, R. M. Pelloux, N. J. Grant, *MTA* **1975**, *6*, 45.

[14] N. Kawagoishi, M. Miyazono, T. Nagano, M. Moriyama, *J. Soc. Mater. Sci., Jpn.* **2009**, *58*, 787.

[15] B. Wang, P. Zhang, Q. Q. Duan, Z. J. Zhang, H. J. Yang, X. W. Li, Z. F. Zhang, *Mater. Sci. Eng. A* **2017**, *707*, 674.

[16] U. Karr, R. Schuller, M. Fitzka, B. Schönbauer, D. Tran, B. Pennings, H. Mayer, *J. Mater. Sci.* **2017**, *52*, 5954.

[17] Y. Murakami, S. Kodama, S. Konuma, *Int. J. Fatigue* **1989**, *11*, 291.

[18] P. Würzinger, R. Rabitsch, W. Meyer, *J. Mater. Sci.* **2004**, *39*, 7295.

[19] J. Damon, T. Hanemann, S. Dietrich, G. Graf, K.-H. Lang, V. Schulze, *Int. J. Fatigue* **2019**, *127*, 395.

[20] A. Gatto, E. Bassoli, L. Denti, *Addit. Manuf.* **2018**, *24*, 13.

[21] A. B. Spierings, M. Schneider, R. Eggenberger, *Rapid Prototyping J.* **2011**, *17*, 380.

[22] F. Deirmina, M. Kearns, P. A. Davies, L. Harris, V. Pekka Matilainen, S. Lövquist, in *Euro PM2020 Proceedings, EPMA*, Virtual Congress Virtual due to Covid 19, **2020**.

[23] F. Deirmina, N. Peghini, B. AlMangour, D. Grzesiak, M. Pellizzari, *Mater. Sci. Eng. A* **2019**, *753*, 109.

[24] E. A. Jägle, P.-P. Choi, J. V. Humbeeck, D. Raabe, *J. Mater. Res.* **2014**, *29*, 2072.

[25] E. A. Jägle, Z. Sheng, P. Kürnsteiner, S. Ocylok, A. Weisheit, D. Raabe, *Materials* **2017**, *10*, 8.

[26] A. Stormvinter, A. Borgenstam, J. Ågren, *Metall. Mater. Trans. A* **2012**, *43*, 3870.

[27] M. Król, P. Snopiński, A. Czech, *J. Therm. Anal. Calorim.* **2020**, *142*, 1011.

[28] T. Hanamura, S. Torizuka, S. Tamura, S. Enokida, H. Takechi, *ISIJ Int.* **2013**, *53*, 2218.

[29] S. Shamsdini, H. Pirgazi, M. H. Ghoncheh, M. Sanjari, B. S. Amirkhiz, L. Kestens, M. Mohammadi, *Addit. Manuf.* **2021**, *41*, 101954.

[30] J. D. Embury, *MTA* **1985**, *16*, 2191.

[31] F. Yan, W. Xiong, E. Faierson, G. B. Olson, *Scr. Mater.* **2018**, *155*, 104.

[32] T. Hong, T. Debroy, S. S. Babu, S. A. David, *Metall. Mater. Trans. B* **2000**, *31*, 161.

[33] T. Hong, T. Debroy, *Metall. Mater. Trans. B* **2003**, *34*, 267.

[34] D. Gu, Y.-C. Hagedorn, W. Meiners, G. Meng, R. J. S. Batista, K. Wissenbach, R. Poprawe, *Acta Mater.* **2012**, *60*, 3849.

[35] S. Floreen, *Metall. Rev.* **1968**, *13*, 115.

[36] R. Casati, J. N. Lemke, A. Tuissi, M. Vedani, *Metals* **2016**, *6*, 218.

[37] T. Karthikeyan, V. T. Paul, S. Saroja, A. Moitra, G. Sasikala, M. Vijayalakshmi, *J. Nucl. Mater.* **2011**, *419*, 256.

[38] S. Gialanella, A. Malandruccolo, in *Aerospace Alloys* (Eds: S. Gialanella, A. Malandruccolo), Springer International Publishing, Cham **2020**, p. 191.

[39] N. Kawagoishi, T. Nagano, M. Moriyama, E. Kondo, *Mater. Manuf. Process.* **2009**, *24*, 1431.

[40] Y. Murakami, M. Endo, *Int. J. Fatigue* **1994**, *16*, 163.

[41] C. Elangeswaran, K. Gurung, R. Koch, A. Cutolo, B. Van Hooreweder, *Fatigue Fract. Eng. Mater. Struct.* **2020**, *43*, 2359.

[42] Y. J. Liu, S. J. Li, H. L. Wang, W. T. Hou, Y. L. Hao, R. Yang, T. B. Sercombe, L. C. Zhang, *Acta Mater.* **2016**, *113*, 56.

[43] Z. Zhang, M. Koyama, M. M. Wang, K. Tsuzaki, C. C. Tasan, H. Noguchi, *Int. J. Fatigue* **2018**, *113*, 126.

[44] X. Ran, D. Liu, J. Li, H. Wang, X. Cheng, J. Zhang, H. Tang, X. Liu, *Mater. Sci. Eng. A* **2018**, *721*, 251.

[45] H. Nakagawa, T. Miyazaki, *J. Mater. Sci.* **1999**, *34*, 3901.

[46] M.-M. Wang, C. C. Tasan, D. Ponge, A. Kostka, D. Raabe, *Acta Mater.* **2014**, *79*, 268.

[47] https://Www. Bohler-Edelstahl. Com/App/Uploads/Sites/92/2020/12/Productdb/Api/W722de. Pdf n.d.